Quasicircular inspirals and plunges from nonspinning effective-one-body Hamiltonians with gravitational self-force information

Andrea Antonelli,[1] Maarten van de Meent,[1] Alessandra Buonanno,[1,2] Jan Steinhoff,[1] and Justin Vines[1]

[1]*Max Planck Institute for Gravitational Physics (Albert Einstein Institute), Am Mühlenberg 1, Potsdam 14476, Germany*

[2]*Department of Physics, University of Maryland, College Park, Maryland 20742, USA*

(Received 11 August 2019; published 7 January 2020)

The self-force program aims at accurately modeling relativistic two-body systems with a small mass ratio (SMR). In the context of the effective-one-body (EOB) framework, current results from this program can be used to determine the effective metric components at linear order in the mass ratio, resumming post-Newtonian (PN) dynamics around the test-particle limit in the process. It was shown in [Akcay *et al.*, Phys. Rev. D **86**, 104041 (2012).] that, in the original (standard) EOB gauge, the SMR contribution to the metric component $g_{tt}^{\rm eff}$ exhibits a coordinate singularity at the light-ring (LR) radius. In this paper, we adopt a different gauge for the EOB dynamics and obtain a Hamiltonian that is free of poles at the LR, with complete circular-orbit information at linear order in the mass ratio and non-circular-orbit and higher-order-in-mass-ratio terms up to 3PN order. We confirm the absence of the LR divergence in such an EOB Hamiltonian via plunging trajectories through the LR radius. Moreover, we compare the binding energies and inspiral waveforms of EOB models with SMR, PN and mixed SMR-3PN information on a quasicircular inspiral against numerical-relativity predictions. We find good agreement between numerical-relativity simulations and EOB models with SMR-3PN information for both equal- and unequal-mass ratios. In particular, when compared to EOB inspiral waveforms with only 3PN information, EOB Hamiltonians with SMR-3PN information improves the modeling of binary systems with small mass ratios $q \lesssim 1/3$, with a dephasing accumulated in ∼30 gravitational-wave (GW) cycles being of the order of few hundredths of a radian up to 4 GW cycles before merger.

DOI: 10.1103/PhysRevD.101.024024

I. INTRODUCTION

Solving the two-body problem in general relativity (GR) remains a challenge of both theoretical interest and astrophysical relevance. Although an analytical solution is lacking, advances in numerical relativity (NR) in the past decades provided the first numerical evolutions of merging compact objects [1–3], as well as catalogs of waveforms [4–8]. On the analytical side of the problem, approximations to the binary motion and gravitational radiation, via expansions in one or more small parameters, have been applied to different domains of validity [9–11], providing us with a variety of waveform models.

The effective-one-body (EOB) framework is a synergistic approach that allows us to resum information from several analytical approximations. NR-calibrated inspiral-merger-ringdown models based on EOB theory [12–16] were employed by LIGO-Virgo experiments to detect gravitational waves (GWs) and infer astrophysical and cosmological information from them [17–25]. In view of the expected increase in the signal-to-noise ratio of signals detected with upcoming LIGO-Virgo runs, and next generation detectors in space (LISA [26]) and on Earth (Einstein Telescope [27] and Cosmic Explorer [28]), it is important and timely to include more physics and build more accurate waveforms in the EOB approach.

Historically, physical information from the two-body problem has mostly entered EOB theory via the post-Newtonian (PN) expansion [29–31], valid for bound orbits at large distances and for velocities smaller than the speed of light $v^2/c^2 \sim GM/rc^2 \ll 1$ (here $M = m_1 + m_2$ is the total mass, with m_1 the mass of the primary and m_2 the mass of the secondary body). PN conservative-dynamics information has so far been calculated up to fourth order, in the nonspinning case, using the Arnowitt-Deser-Misner (ADM) [32–34], Fokker [35–37] and effective-field-theory approaches [38,39] (which were also employed to determine the 5PN gravitational interaction in the static limit [40,41]). In the quasicircular-orbit limit, 4PN information has been successfully included in the EOB dynamics in the form of an expansion in the inverse radius $u \equiv GM/rc^2 \ll 1$ and in the momenta $\mathbf{p}^2$, with exact dependence on the symmetric mass ratio $\nu = m_1 m_2/M^2$ [42]. Further resummations of this PN expansion form the core of the EOB waveform models [12,43–46]. Post-Minkowskian (PM) information, valid in the weak field

$GM/rc^2 \ll 1$, but for all velocities $v^2/c^2 \leq 1$, has also provided valuable insight in the structure of EOB Hamiltonians, for both spinning and nonspinning bound systems [47–51].

The self-force (SF) program, initiated in Refs. [52,53] and based on an expansion of Einstein's equations in the small mass ratio (SMR) $q = m_2/m_1$, has been successful in the calculation of the gravitational SF of a small body around Schwarzschild [54,55], and recently Kerr black holes [56–59], to first order in the mass ratio and for generic bound orbits. The results, corroborated by the use of several gauges and numerical techniques (see, e.g., Ref. [10] and references therein), have been already used to evolve extreme-mass-ratio inspirals (EMRIs) around a Schwarzschild black hole [60,61] and they represent a key input for EMRI waveform modeling schemes recently developed [62] and under development [63].

As the SF program employs different gauge-dependent schemes to obtain its results [10], it is paramount to be able to check results via gauge-invariant quantities, such as the innermost-stable-circular-orbit (ISCO) shift [64], periastron advance [65–67], spin-precession [68–73], tidal invariants [74,75] and the Detweiler redshift [76–81]. For a particle with four-velocity $\tilde{u}^\alpha$ normalized in an effective metric $\tilde{g}_{\alpha\beta} = g^{(0)}_{\alpha\beta} + h^{\rm R}_{\alpha\beta}$ [i.e., moving around a Schwarzschild background $g^{(0)}_{\alpha\beta}$ perturbed by a regularized metric $h^{\rm R}_{\alpha\beta}$ and such that $\tilde{g}_{\alpha\beta}\tilde{u}^\alpha\tilde{u}^\beta = -1 + \mathcal{O}(\nu)$], the Detweiler redshift is defined as the ratio between proper time measured in an orbit around the effective metric $\tilde{g}_{\alpha\beta}$, $d\tilde{\tau}$, and coordinate time, $d\tau$[1]: $z \equiv (\tilde{u}^t)^{-1} = d\tilde{\tau}/d\tau$ [10,76]. Recently, the Detweiler redshift has been used for cross-cultural studies between approximations to the two-body problem in GR [11,76,78,82,83], and it has provided an important benchmark to check PN and SMR results in the small-mass-ratio and weak-field domain, in which both PN and SMR frameworks are expected to be valid. This synergistic program has been extended to NR simulations of equal-mass-ratio binaries with the computation of the Detweiler redshift in Ref. [82].

As pointed out in Ref. [84], gauge-invariant SMR quantities such as the Detweiler redshift can be also used to inform the conservative sector of EOB Hamiltonians [66,84–86]. There are two ways in which this valuable information could be incorporated into the EOB approach: it can be either used to partially determine high-order PN coefficients of EOB Hamiltonians [87–96] or it can be used to resum PN dynamics around the test-body limit [85,86,97]. Here, we focus on the latter approach.

Currently available EOB Hamiltonians informed with the Detweiler redshift cannot be reliably evolved near the Schwarzschild light-ring (LR) radius, i.e., $r = 3GM/c^2$. Such an issue, hereafter called the *LR-divergence* problem, appears as a coordinate singularity of the effective Hamiltonian at the Schwarzschild LR [85,97]. In this paper, we address the problem and, adopting a different EOB gauge, we obtain a Hamiltonian with SMR information that exhibits no divergence at the LR radius. This result allows us to use the precious near-LR, strong-field information from SF calculations in the evolutions of EOB Hamiltonians.

The organization of the paper is as follows. In Sec. II we review the LR divergence arising from informing the conservative sector of standard EOB Hamiltonians with the Detweiler redshift and we discuss how a different EOB gauge (introduced in Ref. [47] in the context of PM calculations) helps to solve the issue. In Sec. III, we inform the conservative sector of EOB Hamiltonians in the alternative gauge with circular-orbit information from the Detweiler redshift, and with both non-circular-orbit and higher-order-in-mass-ratio information from the PN approximation. In Sec. IV, we evolve quasicircular inspirals from this LR-divergence-free Hamiltonian and show that the evolution of the orbital separation crosses the LR radius without encountering singularities. Moreover, we perform systematic comparisons against NR predictions of phase and binding energy for nonspinning systems with mass ratios $1/10 \leq q \leq 1$. We conclude in Sec. V. In the Appendix we present high-precision fits to the Detweiler redshift with improved data in the strong field. We use geometric units $G = c = 1$ throughout the paper.

II. ON GAUGES AND THE LIGHT-RING DIVERGENCE

We begin by noting some conventions to be used in the following sections. In the present paper, we do not consider spinning systems; we denote the reduced mass by $\mu = (m_1 m_2)/M$ and the total mass by $M = m_1 + m_2$. We work with generalized (polar) coordinates $q_a \equiv (r, \phi)$ in the orbital plane, with canonically conjugate momenta $p_a \equiv (p_r, p_\phi)$, and we often employ the mass-reduced inverse orbital separation $u \equiv M/r$ and the mass-reduced momenta $\hat{p}_r \equiv p_r/\mu$ and $\hat{p}_\phi \equiv p_\phi/(M\mu)$.

A. The light-ring divergence

In the EOB approach, the real two-body motion is mapped to the effective motion of a test body in an effective *deformed*-Schwarzschild spacetime with coordinates (t, r, θ, ϕ), with the deformation parameter being the symmetric mass ratio ν. The mapping can be obtained via a

[1]As pointed out in Ref. [10], z does not correspond to the gravitational redshift due to the use of the regularized perturbation $h^{\rm R}_{\alpha\beta}$ in its definition. It does only in the full geometry, e.g., including a singular metric $h^{\rm S}_{\alpha\beta}$ at the location of the particle such that the body perturbation is $h_{\alpha\beta} \equiv h^{\rm R}_{\alpha\beta} + h^{\rm S}_{\alpha\beta}$. A sounder physical description can be obtained if the small companion is a black hole, since the Detweiler redshift can then be linked to the surface gravity κ of the small body [82].

dictionary between the action integrals $I_a = (2\pi)^{-1} \oint p_a dq_a$ of a two-body system in the center-of-mass frame and those of a test body moving in the effective metric $g^{\rm eff}_{\mu\nu}$. Considering orbits in the equatorial plane $\theta = \pi/2$, identifying the radial and angular action integrals of real and effective systems, i.e., setting $I^{\rm real}_{\rm r} = I^{\rm eff}_{\rm r}$ and $I^{\rm real}_{\phi} = I^{\rm eff}_{\phi}$, the EOB approach allows a simple relation between the real $H_{\rm EOB}(r, p_r, p_\phi, \nu)$ and effective $H_{\rm eff}(r, p_r, p_\phi, \nu)$ Hamiltonians [29]:

$$H_{\rm EOB} \equiv M\hat{H}_{\rm EOB} = M\sqrt{1 + 2\nu\left(\frac{H_{\rm eff}}{\mu} - 1\right)}. \tag{2.1}$$

$H_{\rm eff}$ describes the motion of a test body with mass μ and is determined by a mass-shell constraint of the form [31]

$$g^{\mu\nu}_{\rm eff} p_\mu p_\nu + \mu^2 + Q(r, p_r, p_\phi, \nu) = 0, \tag{2.2}$$

where the effective metric is given by

$$ds^2 = -A(r,\nu)dt^2 + [A(r,\nu)\bar{D}(r,\nu)]^{-1}dr^2 + r^2 d\Omega^2, \tag{2.3}$$

with the potentials $A(r,\nu)$ and $\bar{D}(r,\nu)$ depending on the orbital separation r and the symmetric mass ratio ν. In terms of the inverse radius $u = M/r$, they reduce to $A_0(u) = 1–2u$ and $\bar{D}_0 = 1$ in the test-particle limit ($\nu \to 0$). Inserting the inverse of the metric (2.3) into Eq. (2.2), and using $p_\mu = (-H_{\rm eff}, p_r, p_\theta = 0, p_\phi)$, the mass-reduced effective Hamiltonian $\hat{H}_{\rm eff} \equiv H_{\rm eff}/\mu$ is found to be [31]

$$\hat{H}^2_{\rm eff} = A(u,\nu)[1 + \hat{p}^2_\phi u^2 + A(u,\nu)\bar{D}(u,\nu)\hat{p}^2_r + \hat{Q}(u, \hat{p}_r, \hat{p}_\phi, \nu)], \tag{2.4}$$

with $\hat{Q} \equiv Q/\mu^2$. The nongeodesic function Q in Eq. (2.2) has been introduced to extend the EOB Hamiltonian through 3PN order without changing the mapping (2.1) [for a geodesic one-body motion at 3PN order with an energy map different from (2.1) see Appendix A in Ref. [31]]. Its mass-reduced form $\hat{Q}(u, \hat{p}_r, \hat{p}_\phi, \nu)$ in Eq. (2.4) generically depends on both the mass-reduced radial momentum $\hat{p}_r$ and the mass-reduced angular momentum $\hat{p}_\phi$. Reference [31] showed that at 3PN order $\hat{Q}$ must be fourth order in the momenta, and that the nongeodesic term is not uniquely fixed. By setting some of the free parameters to zero, it is possible to make the function $\hat{Q}(u, \hat{p}_r, \hat{p}_\phi, \nu)$ depend only on the radial momentum [i.e., $\hat{Q}(u, \hat{p}_r, \hat{p}_\phi, \nu) \to \hat{Q}(u, \hat{p}_r, \nu)$]. Since 2000, this choice of $\hat{Q}$ has been adopted in several EOB papers (although see Refs. [98,99] for alternative choices of $\hat{Q}$). Henceforth, we shall denote the $\hat{Q}$ function that only depends on the radial momentum as $\hat{Q}^{\rm DJS}(u, \hat{p}_r, \nu)$, after the initials of the three authors of Ref. [31]. We refer to the DJS EOB Hamiltonian as the Hamiltonian that uses the $\hat{Q}^{\rm DJS}(u, \hat{p}_r, \nu)$ function. Note that in this gauge, the angular momentum $\hat{p}_\phi$ only appears in the second term in brackets in Eq. (2.4). Moreover, in the circular-orbit limit ($\hat{p}_r = 0$) the conservative-dynamics information is fully described by the $A(u,\nu)$ potential in this gauge, as found at 2PN order [29]. The 4PN expressions for $A(u,\nu)$, $\bar{D}(u,\nu)$ and $\hat{Q}^{\rm DJS}(u, \hat{p}_r, \nu)$ in the DJS gauge, for quasicircular orbits, are obtained mapping Eq. (2.1) to the 4PN-expanded Hamiltonian and can be found in Ref. [42].

The first efforts to incorporate SMR quantities in EOB Hamiltonians sought to do so using the gauge of Eq. (2.4) with $\hat{Q}(u, \hat{p}_r, \hat{p}_\phi, \nu) \to \hat{Q}^{\rm DJS}(u, \hat{p}_r, \nu)$ [65,86,97,100]. In this gauge, the function $A(u,\nu)$, having the complete dynamical information for circular orbits, allows a linear-in-ν expansion about the Schwarzschild limit:

$$A(u,\nu) = 1 - 2u + \nu a(u) + \mathcal{O}(\nu^2). \tag{2.5}$$

The $a(u)$ function resums the complete circular-orbit PN dynamics in linear order in ν. References [85,86] obtained an expression for $a(u)$ employing the linear-in-ν correction to the Detweiler redshift. Notably, the Detweiler redshift is expanded around the Schwarzschild background, $z(x) = \sqrt{1-3x} + \nu\Delta z(x) + \mathcal{O}(\nu^2)$ [where $x \equiv (M\Omega)^{2/3}$ is the gauge-independent inverse radius], and the Δz correction is linked to $a(u)$ via the first law of binary-black-hole mechanics [83]. The resulting expression reads

$$a(u) = \Delta z(u)\sqrt{1-3u} - u\left(1 + \frac{1-4u}{\sqrt{1-3u}}\right). \tag{2.6}$$

In Eq. (2.6), Δz depends on the gauge-dependent inverse radius u, rather than its gauge-independent counterpart x. This is only correct if we restrict to first order in ν, since $x = u + \mathcal{O}(\nu)$. The quantity $\Delta z(x)$, has been fitted with data extending to the LR [97], allowing precious strong-field information to enter the EOB dynamics.

The form of $a(u)$ is suggestive of trouble arising at the Schwarzschild light ring, i.e., at $u_{\rm LR} = 1/3$, where the second term in Eq. (2.6) diverges. In principle, this divergence might be tamed by the behavior of the redshift $\Delta z(u)$ appearing in the first term in brackets, but data for the redshift up to the LR show that this is not the case and that $a(u)$ indeed diverges there [97]. This is worrisome, as $a(u)$ directly enters the effective Hamiltonian and, via the energy map, the EOB-resummed dynamics. The EOB dynamics thus contains a divergence *for generic orbits* (e.g., for any value of $\hat{p}_\phi$ and $\hat{p}_r$). It was pointed out in Ref. [97] that the LR divergence is a phase-space coordinate singularity that arises due to the use of the DJS

gauge, and that can be solved adopting a different gauge in which the function $\hat{Q}$ grows as $\hat{Q} \propto \hat{p}_\phi^3$ when $\hat{p}_\phi \to \infty$ and $\hat{p}_r \to 0$.

It is worth mentioning that the argument in Ref. [97] stems from a similar LR divergence that has appeared when including tidal effects in the EOB approach [101]. Tidal effects enter the potential $A(u)$ via a correction in a tidal expansion akin to Eq. (2.5): $A(u) = A_{2\,\mathrm{pp}} + \mu_\mathrm{T} a_\mathrm{T}(u,\nu) + \mathcal{O}(\mu_\mathrm{T}^2)$, where $A_{2\,\mathrm{pp}}$ is the two point-particle (pp) EOB potential [101] and μ_T the small tidal parameter. It has been found in Ref. [101] that, in the extreme-mass-ratio limit and for circular orbits, the first-order correction scales as $a_\mathrm{T}(u,\nu) \propto (1-3u)^{-1}$ when $u \to u_\mathrm{LR}$. An alternative EOB Hamiltonian that includes dynamical tides without introducing poles at the LR has been introduced in Ref. [102]; this has been achieved by abandoning the DJS gauge (see, e.g., their Appendix D).

B. The post-Schwarzschild effective-one-body gauge

Reference [47] has shown that it is possible to obtain a different EOB gauge, hereafter the *post-Schwarzschild* (PS) gauge, solving Eq. (2.2) with the Schwarzschild limit of the metric (2.3). The mass-reduced effective Hamiltonian thus obtained has the following form:

$$\hat{H}_\mathrm{eff}^\mathrm{PS} = \sqrt{\hat{H}_\mathrm{S}^2 + (1-2u)\hat{Q}^\mathrm{PS}(u,\nu,\hat{H}_\mathrm{S})}, \tag{2.7}$$

where $\hat{H}_\mathrm{S}$ is the Schwarzschild Hamiltonian:

$$\hat{H}_\mathrm{S}(u,\hat{p}_r,\hat{p}_\phi) = \sqrt{(1-2u)[1+\hat{p}_\phi^2 u^2 + (1-2u)\hat{p}_r^2]}. \tag{2.8}$$

In Ref. [47], the PS function $\hat{Q}^\mathrm{PS}$ has been derived to 2PM order via a scattering-angle calculation and to 3PN order via a canonical transformation from the DJS Hamiltonian at 3PN. In Ref. [51], these calculations have been extended to 3PM and 4PN orders, respectively (the latter only in the near-circular-orbit limit).

It is noticed that, in PS EOB Hamiltonians, all the information on the two-body problem with $\nu \neq 0$ is contained in $\hat{Q}^\mathrm{PS}(u,\nu,\hat{H}_\mathrm{S})$. This feature and the fact that circular-orbit dynamics is contained also in the $\hat{Q}$ function, significantly differentiate PS Hamiltonians from DJS ones. The PS gauge is uniquely fixed resumming the angular and radial momenta into the Schwarzschild Hamiltonian (2.8). The powers of such momenta are furthermore not bound in any way, due to the generic functional dependence of $\hat{Q}^\mathrm{PS}(u,\nu,\hat{H}_\mathrm{S})$ on $\hat{H}_\mathrm{S}$. In principle, then, arbitrary powers of $\hat{p}_\phi$ are contained in $\hat{Q}^\mathrm{PS}(u,\nu,\hat{H}_\mathrm{S})$ via $\hat{H}_\mathrm{S}$. In particular, differently from $\hat{Q}^\mathrm{DJS}(u,\nu,\hat{p}_r)$, powers of momentum enter at second order in $\hat{Q}^\mathrm{PS}(u,\nu,\hat{H}_\mathrm{S})$ instead of fourth order.

The unconstrained dependence of $\hat{Q}^\mathrm{PS}$ on $\hat{H}_\mathrm{S}$ makes the use of PS Hamiltonians very appealing in the context of our work. It was shown in Ref. [47] that, in the high energy limit for which $\hat{p}_\phi \to \infty$, the LR divergence can be captured by the coefficient of a term proportional to $\hat{H}_\mathrm{S}^3$. This result is in agreement with a point made in the conclusions of Ref. [97]. As it approaches the LR radius, the effective mass moving in a deformed-Schwarzschild background described by Eqs. (2.5) and (2.6) has a divergent-energy behavior that must be removed with an appropriate energy-corrected mass-ratio parameter $\tilde{\nu} = \nu\hat{H}_\mathrm{S}$. In the next section, building from this knowledge and making use of a simple ansatz for $\hat{Q}^\mathrm{PS}(u,\nu,\hat{H}_\mathrm{S})$, we construct a Hamiltonian in the PS gauge that contains information from Δz, while remaining analytic at the LR.

III. CONSERVATIVE DYNAMICS OF POST-SCHWARZSCHILD HAMILTONIANS

A. Information from circular orbits

In this section, we link the conservative sector of the PS EOB Hamiltonian to the SMR contribution to Δz. Following Ref. [86], we do so matching, at fixed frequency, the circular-orbit binding energy at linear order in ν from the EOB Hamiltonian with the binding energy in the same limit from SF results. The latter is obtained in Ref. [85] and is a consequence of the first law of binary-black-hole mechanics. As a function of Δz and the gauge-invariant inverse radius x, it reads [85]

$$\hat{E}_\mathrm{bind}^\mathrm{SF} = \frac{1-2x}{\sqrt{1-3x}} - 1 + \nu\hat{E}_\mathrm{SMR}(x,\Delta z,\Delta z') + \mathcal{O}(\nu^2), \tag{3.1}$$

$$\hat{E}_\mathrm{SMR}(x,\Delta z,\Delta z') = -1 + \sqrt{1-3x} - \frac{x}{3}\Delta z'(x) + \frac{\Delta z(x)}{2} + \frac{(7-24x)x}{6(1-3x)^{3/2}}. \tag{3.2}$$

The prime denotes differentiation with respect to x. We find it useful to rewrite the redshift as

$$\Delta z(x) = \frac{\Delta z^{(0)}(x)}{1-3x} + \frac{\Delta z^{(1)}(x)}{\sqrt{1-3x}} + \frac{\Delta z^{(2)}(x)}{1-3x}\ln E_\mathrm{S}^{-2}(x). \tag{3.3}$$

In the above expression, we have defined $E_\mathrm{S}(x) \equiv (1-2x)/\sqrt{1-3x}$. In Appendix, $\Delta z^{(0)}(x)$, $\Delta z^{(1)}(x)$ and $\Delta z^{(2)}(x)$ are fitted to high-precision SF data and such to be analytic at the LR. Equation (3.2) then reads

$$\hat{E}_{\rm SMR} = \sqrt{1-3x} - 1 + \frac{(7-24x)x}{6(1-3x)^{3/2}} + \frac{1}{2(1-3x)}\left[\Delta z^{(0)}(x) + \Delta z^{(1)}(x)\sqrt{1-3x} + \Delta z^{(2)}(x)\ln E_{\rm S}^{-2}(x)\right] - \frac{x}{3(1-3x)}\left\{\frac{3\Delta z^{(0)}(x)}{1-3x} + \frac{3\Delta z^{(1)}(x)}{2\sqrt{1-3x}} + \left[\frac{1-6x}{(1-2x)(1-3x)} + \frac{3\ln E_{\rm S}^{-2}(x)}{(1-3x)}\right]\Delta z^{(2)}(x) + (\Delta z^{(0)})'(x) + \sqrt{1-3x}(\Delta z^{(1)})'(x) + (\Delta z^{(2)})'(x)\ln E_{\rm S}^{-2}(x)\right\}. \tag{3.4}$$

For the remainder of this section, we consider the PS EOB Hamiltonian $H_{\rm EOB}$, i.e., Eq. (2.1) with $H_{\rm eff}/\mu$ replaced by $\hat{H}_{\rm eff}^{\rm PS}$ of Eq. (2.7). We propose an ansatz for $\hat{Q}^{\rm PS}$ of the following form:

$$\hat{Q}_{\rm SMR}^{\rm PS}(u,\nu,\hat{H}_{\rm S}) = \nu[f_0(u)\hat{H}_{\rm S}^5 + f_1(u)\hat{H}_{\rm S}^2 + f_2(u)\hat{H}_{\rm S}^3\ln\hat{H}_{\rm S}^{-2}]. \tag{3.5}$$

In the rest of this section, when matching to the SMR results, we limit to circular orbits; thus we use $\hat{H}_{\rm S}(u,\hat{p}_r = 0,\hat{p}_\phi)$ in Eq. (3.5). The role of the $\hat{H}_{\rm S}^5$ term is to capture the global divergence $(1-3x)^{-2}$ of Eq. (3.4),[2] while the second term $\hat{H}_{\rm S}^2$ is devised to incorporate the $\sqrt{1-3x}$ terms appearing in the numerator of the same equation, which would make the Hamiltonian imaginary after the light ring. The term proportional to $\ln\hat{H}_{\rm S}^{-2}$ incorporates the logs in the fit that would make the Hamiltonian nonsmooth at the light ring. Setting $p_r = 0$ and using

$$\dot{p}_r = -\frac{\partial H_{\rm EOB}}{dr}(r, p_r = 0, p_\phi^{\rm circ}, \nu) = 0, \tag{3.6}$$

the (mass-reduced) circular-orbit momentum $\hat{p}_\phi^{\rm circ}$ as a function of the inverse radius u is determined at linear order in ν [with $f_i'(u) = df_i/du$]:

$$\hat{p}_\phi^{\rm circ}(u,\nu) = \frac{1}{\sqrt{u(1-3u)}} + \nu\frac{(1-2u)^2}{4(1-3u)^3\sqrt{u}}[2(1-2u)^3 f_0(u) + 2(1-3u)^{3/2}f_1(u) + 2(1-2u)(1-3u)f_2(u)\ln E_{\rm S}^{-2}(u) - (1-2u)^4 f_0'(u) - (1-2u)(1-3u)^{3/2}f_1'(u) - (1-2u)^2(1-3u)\ln E_{\rm S}^{-2}(u)f_2'(u)] + \mathcal{O}(\nu^2). \tag{3.7}$$

We further use the relation:

$$\Omega = \frac{\partial H_{\rm EOB}}{dp_\phi}(r, p_r = 0, p_\phi^{\rm circ}, \nu), \tag{3.8}$$

and exploit its link to the gauge-independent inverse radius x given by $x = (M\Omega)^{2/3}$. Inserting Eq. (3.7) in Eq. (3.8) and inverting the obtained expression at linear order in ν, we establish a link between the gauge-dependent u and the gauge-independent x inverse radii:

$$u^{\rm circ}(x,\nu) = x + \frac{x\nu}{6(1-3x)^{3/2}}\left\{4 - 20x + 24x^2 - (4-12x)\sqrt{1-3x} - 10(1-2x)^4 f_0(x) - 4\sqrt{1-3x}(1-5x+6x^2)f_1(x) + [4 - 28x + 64x^2 - 48x^3 - (6 - 42x + 96x^2 - 72x^3)\ln E_{\rm S}^{-2}(x)]f_2(x) + (1 - 10x + 40x^2 - 80x^3 + 80x^4 - 32x^5)f_0'(x) + \sqrt{1-3x}(1 - 7x + 16x^2 - 12x^3)f_1'(x) + (1 - 9x + 30x^2 - 44x^3 + 24x^4)\ln E_{\rm S}^{-2}(x)f_2'(x)\right\} + \mathcal{O}(\nu^2). \tag{3.9}$$

To calculate the (mass-reduced) gauge-invariant, circular-orbit binding energy at linear order in ν from $H_{\rm EOB}$, we employ the definition:

$$\hat{E}_{\rm bind}^{\rm EOB} \equiv (H_{\rm EOB} - M)/\mu. \tag{3.10}$$

[2]In principle, a $\hat{H}_{\rm S}^3$ term will suffice to capture the divergence. However, we find that this minimal choice leads to evolutions that are not well behaved for systems with comparable masses.

Inserting Eqs. (3.7) and (3.9) in $H_{\rm EOB}$ and retaining only terms up to first order in the mass ratio, we get

$$\begin{aligned}\hat{E}^{\rm EOB}_{\rm bind}(x,\nu) = {}& \frac{1-2x}{\sqrt{1-3x}} - 1 - \frac{\nu}{6(1-3x)^3}\{(1-3x)(6-37x+59x^2-12x^3) - 2(1-3x)^{3/2}(3-14x+12x^2) \\ & - (3-7x-18x^2)(1-2x)^4 f_0(x) - (1-3x)^{3/2}(3-16x+20x^2) f_1(x) \\ & + (1-3x)(1-2x)^2[2x(1-6x) - (3-9x-6x^2)\ln E_{\rm S}^{-2}(x)] f_2(x) + 2x(1-2x)^5(1-3x) f_0'(x) \\ & + 2x(1-3x)^{5/2}(1-2x)^2 f_1'(x) + 2x(1-3x)^2(1-2x)^3 \ln E_{\rm S}^{-2}(x) f_2'(x)\} + \mathcal{O}(\nu^2). \end{aligned} \tag{3.11}$$

Matching Eq. (3.1) [with correction given by Eq. (3.4)] and Eq. (3.11), we obtain differential equations to be solved for $f_0(x)$, $f_1(x)$ and $f_2(x)$. Further splitting the f_i coefficients as follows:

$$f_0(x) = \tilde{f}_0(x) + \sum_{i=0}^{i=2} f_0^{(i)}(x)\Delta z^{(i)}(x) \tag{3.12}$$

$$f_1(x) = \tilde{f}_1(x) + \sum_{i=0}^{i=2} f_1^{(i)}(x)\Delta z^{(i)}(x), \tag{3.13}$$

$$f_2(x) = \tilde{f}_2(x) + \sum_{i=0}^{i=2} f_2^{(i)}(x)\Delta z^{(i)}(x), \tag{3.14}$$

and imposing that the Hamiltonian coefficients be analytic at the LR radius [i.e., that they do not contain $\sqrt{1-3x}$ or $\ln E_{\rm S}^{-2}(x)$ terms], we obtain the following nonzero solutions[3]:

$$\tilde{f}_0(x) = -\frac{x(1-3x)(1-4x)}{(1-2x)^5}, \tag{3.15a}$$

$$\tilde{f}_1(x) = -\frac{x}{(1-2x)^2}, \tag{3.15b}$$

$$f_0^{(0)}(x) = \frac{1-3x}{(1-2x)^5}, \tag{3.15c}$$

$$f_1^{(1)}(x) = \frac{1}{(1-2x)^2}, \tag{3.15d}$$

$$f_2^{(2)}(x) = \frac{1}{(1-2x)^3}. \tag{3.15e}$$

[3]Similarly to what is done in Ref. [86], we impose that the PN expansion cannot admit half-integer powers of x. This allows us to set all constants of integration to zero.

The $f_i(x)$ coefficients are readily found via Eqs. (3.12), (3.13) and (3.14) and then inserted in the nongeodesic term in the effective Hamiltonian (3.5) to obtain

$$\begin{aligned}\frac{\hat{Q}^{\rm PS}_{\rm SMR}}{\nu}(u,\nu,\hat{H}_{\rm S}) = {}& (1-3u)\left[\frac{\Delta z^{(0)}(u)}{(1-2u)^5} - \frac{(1-4u)u}{(1-2u)^5}\right]\hat{H}_{\rm S}^5 \\ & + \left[\frac{\Delta z^{(1)}(u)}{(1-2u)^2} - \frac{u}{(1-2u)^2}\right]\hat{H}_{\rm S}^2 \\ & + \frac{\Delta z^{(2)}(u)}{(1-2u)^3}\hat{H}_{\rm S}^3 \ln \hat{H}_{\rm S}^{-2}. \end{aligned} \tag{3.16}$$

We see that the resulting Hamiltonian concisely resums the complete circular-orbit PN dynamics at linear order in ν. The nongeodesic function $\hat{Q}^{\rm PS}_{\rm SMR}$ does not contain any term divergent at the LR, as $\Delta z^{(0)}(u)$, $\Delta z^{(1)}(u)$ and $\Delta z^{(2)}(u)$ are constructed to be analytic there.

B. Information from noncircular orbits and from higher orders in the mass ratio

The calculation in Sec. III A is carried out in the circular-orbit limit at linear order in the mass ratio. However, it is possible to include more physical information to the Hamiltonian, coming both from non-circular-orbit terms and from terms at higher orders in the mass ratio. For instance, self-force information for mildly eccentric orbits can be obtained via the SMR correction to the periastron advance $\rho_{\rm SF}$ [65], which can then be linked to the EOB potentials. This was the strategy used in Refs. [84,86] to obtain an expression for the potential $\bar{D}(r)$ in terms of $\Delta z(u)$ and $\rho_{\rm SF}(u)$ and introduce noncircular SF data into the EOB Hamiltonian up to the Schwarzschild ISCO (i.e., $u_{\rm ISCO} = 1/6$). Alternatively, one can exploit the generalized redshift [77] and link it to $\bar{D}(r)$, as done in Refs. [100,103]. Here, we insert generic-orbit PN information in our Hamiltonian and leave the inclusion of noncircular SMR information in $\hat{Q}^{\rm PS}$ to future work.

Post-Schwarzschild EOB Hamiltonians with PN information from generic orbits have been already considered in the literature. For example, the PS Hamiltonian at 3PN order has been investigated in Ref. [47]. Using the PN

parameters $Y \equiv (\hat{H}_S^2 - 1) \sim \mathcal{O}(1/c^2)$ and u, its expression is given by

$$\hat{Q}^{\rm PS}_{\rm 3PN} = 3\nu u^2 Y + 5\nu u^3 + \left(3\nu - \frac{9}{4}\nu^2\right) u^2 Y^2 + \left(27\nu - \frac{23}{4}\nu^2\right) u^3 Y + \left(\frac{175}{3}\nu - \frac{41\pi^2}{32}\nu - \frac{7}{2}\nu^2\right) u^4. \quad (3.17)$$

As discussed, the above Hamiltonian contains two-body information that is not captured by the calculation leading to $\hat{Q}^{\rm PS}_{\rm SMR}$ and that we wish to add to it.

To this end, we consider a mixed SMR-3PN nongeodesic function of the following form:

$$\hat{Q}^{\rm PS}_{\rm SMR\text{-}3PN} = \hat{Q}^{\rm PS}_{\rm SMR} + \Delta\hat{Q}^{\rm PS}, \quad (3.18)$$

where $\hat{Q}^{\rm PS}_{\rm SMR}$ is given by Eq. (3.16) and contains all the circular-orbit terms at linear order in ν, while $\Delta\hat{Q}^{\rm PS}$ is fixed demanding that it contains all the additional PN information from Eq. (3.17), in such a way not to contribute to the linear-in-ν binding energy in the circular-orbit limit.

We opt to further split $\Delta\hat{Q}^{\rm PS}$ into two contributions: $\Delta\hat{Q}^{\rm PS}_{\rm extra}$ collects the extra terms up to 3PN order (including both noncircular 3PN terms at linear order in ν and ν^2 terms), while $\Delta\hat{Q}^{\rm PS}_{\rm count}$ is a counterterm whose functionality is explained below. We then have

$$\Delta\hat{Q}^{\rm PS} \equiv \Delta\hat{Q}^{\rm PS}_{\rm extra} - \Delta\hat{Q}^{\rm PS}_{\rm count}. \quad (3.19)$$

The former contribution is readily obtained calculating the difference between Eq. (3.17) and the 3PN expansion of Eq. (3.16).[4] The result reads

$$\Delta\hat{Q}^{\rm PS}_{\rm extra} = 3\nu u^2 Y + \left(3\nu - \frac{9}{4}\nu^2\right) u^2 Y^2 + 3\nu u^3 + \left(22\nu - \frac{23}{4}\nu^2\right) u^3 Y + \left(16\nu - \frac{7}{2}\nu^2\right) u^4. \quad (3.20)$$

In the PS gauge, $\hat{Q}^{\rm PS}$ depends on momenta via $\hat{H}_S(u, \hat{p}_r, \hat{p}_\phi)$, which cannot be separated into circular and noncircular-orbit contributions. Because of that, the linear-in-ν portion of Eq. (3.20) contributes to the linear-in-ν binding energy for circular orbits. Therefore, the addition of $\Delta\hat{Q}^{\rm PS}_{\rm extra}$ to $\Delta\hat{Q}^{\rm PS}_{\rm SMR}$ spoils the matching between EOB and SF binding energies for circular orbits at linear order in the mass ratio guaranteed by the sole presence of $\Delta\hat{Q}^{\rm PS}_{\rm SMR}$.

The matching between the two binding energies can be maintained with a particular choice of the second contribution to Eq. (3.19), i.e., $\Delta\hat{Q}^{\rm PS}_{\rm count}$. We choose a counterterm that starts at 4PN, in order not to spoil the agreement at 3PN for generic orbits guaranteed by Eq. (3.20):

$$\Delta\hat{Q}^{\rm PS}_{\rm count} = \nu[q_{(3,2)} u^3 Y^2 + q_{(4,1)} u^4 Y + q_{(5,0)} u^5]. \quad (3.21)$$

We impose that the linear-in-ν binding energy from $\Delta\hat{Q}^{\rm PS}$ from Eq. (3.19) [calculated as done for Eq. (3.11) in Sec. III A] vanishes and we obtain

$$q_{(3,2)} = 9; \qquad q_{(4,1)} = 96; \qquad q_{(5,0)} = 112. \quad (3.22)$$

The final PN correction $\Delta\hat{Q}^{\rm PS}$ thus contains all the extra information from generic orbits at 3PN that is not captured by $\hat{Q}^{\rm PS}_{\rm SMR}$, without contributing to the linear in mass-ratio binding energy for circular orbits. The exercise above can be repeated at one PN order higher to obtain $\Delta\hat{Q}^{\rm PS}$ at 4PN starting from the 4PN EOB Hamiltonian in the PS gauge. [51]. Such a computation does not present major differences from the calculation above: the only feature changing is the counterterm, which needs to start at 5PN and include logarithmic terms. We have decided not to include $\Delta\hat{Q}^{\rm PS}$ at 4PN in this paper, as the 4PN Hamiltonian from which it is constructed is only valid for near-circular orbits. The $\Delta\hat{Q}^{\rm PS}$ at 3PN that we obtain here is instead valid for generic orbits.

IV. INSPIRALS IN EFFECTIVE-ONE-BODY THEORY

A. Plunging through the light ring with small-mass-ratio Hamiltonians

In this section, we evolve the EOB Hamiltonians constructed in Secs. III A and III B [i.e., Eq. (2.7) with nongeodesic functions (3.16) and (3.18)], and the EOB Hamiltonian with SMR information in the DJS gauge. We refer to them as $H^{\rm EOB,PS}_{\rm SMR}$, $H^{\rm EOB,PS}_{\rm SMR\text{-}3PN}$ and $H^{\rm EOB}_{\rm SMR}$, see Table I (which also includes our notation for the PN Hamiltonians in both DJS and PS gauges).

TABLE I. Two-body EOB Hamiltonians.

$H^{\rm EOB,PS}_{\rm SMR}$	SMR Hamiltonian in PS gauge	This paper
$H^{\rm EOB,PS}_{\rm SMR\text{-}3PN}$	SMR-3PN Hamiltonian in PS gauge	This paper
$H^{\rm EOB}_{\rm SMR}$	SMR Hamiltonian in the DJS gauge (with LR divergence)	[86]
$H^{\rm EOB,PS}_{n\rm PN}$	nPN Hamiltonian in PS gauge	[47]
$H^{\rm EOB}_{n\rm PN}$	nPN Hamiltonian in DJS gauge	[29,31]

[4]That is, Eq. (3.16) is expanded in the PN parameters u and $Y = \hat{H}_S^2 - 1$. The redshift functions $\Delta z^{(0)}(u)$, $\Delta z^{(1)}(u)$ and $\Delta z^{(2)}(u)$ also need to be PN expanded: their expressions are obtained matching the 3PN expansion of the redshift from Ref. [89] and Eq. (3.3).

The EOB approach is comprised of a conservative sector, discussed in detail in Sec. II, and a dissipative sector, responsible for the slow GW-driven inspiral of the compact bodies towards merger. The basic set of equations for inspiraling orbits in the EOB framework are the Hamilton equations augmented with a radiation-reaction force $\mathcal{F}_{\rm RR}$. In terms of a generic mass-reduced EOB Hamiltonian $\hat{H}^{\rm EOB}(\hat{r}, \hat{p}_{r_*}, \hat{p}_\phi)$, the equations read [12,30,99,104]

$$\frac{d\hat{r}}{d\hat{t}} = \frac{A(\hat{r})}{\sqrt{D(\hat{r})}} \frac{\partial \hat{H}^{\rm EOB}}{\partial \hat{p}_{r_*}}, \tag{4.1a}$$

$$\frac{d\phi}{d\hat{t}} = \frac{\partial \hat{H}^{\rm EOB}}{\partial \hat{p}_\phi}, \tag{4.1b}$$

$$\frac{d\hat{p}_{r_*}}{d\hat{t}} = -\frac{A(\hat{r})}{\sqrt{D(\hat{r})}} \frac{\partial \hat{H}^{\rm EOB}}{\partial \hat{r}} + \mathcal{F}_{\rm RR} \frac{\hat{p}_{r_*}}{\hat{p}_\phi}, \tag{4.1c}$$

$$\frac{d\hat{p}_\phi}{d\hat{t}} = \mathcal{F}_{\rm RR}, \tag{4.1d}$$

where we have introduced the mass-reduced radius $\hat{r} \equiv r/M$ and coordinate time $\hat{t} \equiv t/M$ and used the mass-reduced radial momentum $\hat{p}_{r_*}$ conjugate to the radius r_* in tortoise coordinates, defined for generic potentials $A(\hat{r})$ and $D(\hat{r})$[5] by

$$\frac{d\hat{r}_*}{d\hat{r}} \equiv \frac{\sqrt{D(\hat{r})}}{A(\hat{r})} = \frac{\hat{p}_r}{\hat{p}_{r_*}}. \tag{4.2}$$

In the evolution of the EOB Hamiltonian in the DJS gauge we use the PN-expanded expressions for $A(\hat{r})$, $D(\hat{r})$ and $\hat{Q}^{\rm DJS}$ at the required PN order [29,31,42] (i.e., we use their 2PN and 3PN expressions in the evolutions of $H^{\rm EOB}_{\rm 2PN}$ and $H^{\rm EOB}_{\rm 3PN}$, respectively), whereas we use their test-body limits in the evolutions of Hamiltonians in the PS gauge.[6] The Hamiltonians in both gauges depend on $\hat{p}_{r_*}$, rather than $\hat{p}_r$.

The radiation-reaction force $\mathcal{F}_{\rm RR}$ drives the inspiral of the system and it contains semianalytical two-body information [43,104,105]. In this paper, we employ its non-Keplerian form (with $\hat{\Omega} \equiv d\phi/d\hat{t} = M\Omega$):

$${}^{\rm nK}\mathcal{F}_{\rm RR} = -\frac{1}{\nu \hat{\Omega}} \frac{dE}{dt}, \tag{4.3}$$

where dE/dt is the GW flux for quasicircular orbits [43]:

$$\frac{dE}{dt} = \frac{\hat{\Omega}^2}{8\pi} \sum_{l=2}^{l_{\rm max}=8} \sum_{m=l-2}^{l} m^2 |\hat{r} h_{lm}|^2. \tag{4.4}$$

The modes h_{lm} are built from PN theory, but resummed multiplicatively (see e.g., Ref. [43]). Here, we use the resummation of the (nonspinning) modes and flux presented in Ref. [12] (which coincides with the state-of-the-art modes and flux used in the EOB waveform model for LIGO/Virgo data analysis [15], when spins are set to zero). We do not include the "next-to-quasi-circular" (NQC) coefficients [15], or any calibration parameter obtained imposing better agreement with numerical-relativity waveforms. Our main motivation here is to compare how well the conservative EOB dynamics of SMR models compare to PN ones and with NR.

The result of the evolved orbital separations $\hat{r}$ of both DJS and PS Hamiltonians for $q = 1/10$ are reported in Fig. 1. Focusing on the evolution in the DJS case, it is seen that the pole in the conservative part of the DJS Hamiltonian affects the motion of the effective body close to the LR radius. That is, $H^{\rm EOB}_{\rm SMR}$ diverges at $\hat{r}^{\rm LR}_{\rm S} = 3$, at which point it acts as an infinite potential barrier that the effective mass cannot cross. Conversely, the effective mass plunges through the Schwarzschild LR radius in the cases of $H^{\rm EOB,PS}_{\rm SMR}$ and $H^{\rm EOB,PS}_{\rm SMR\text{-}3PN}$. This finding confirms that there is no unphysical behavior at the LR radius for SMR Hamiltonians in the PS gauge. To conclude, we also notice that the evolutions of the $H^{\rm EOB,PS}_{\rm SMR}$ and $H^{\rm EOB,PS}_{\rm SMR\text{-}3PN}$ models (red and blue dots) stop soon after the LR radius. In principle we would expect them to stop at the Schwarzschild horizon ($u = 1/2$). This is not the case in Fig. 1. In the PS gauge, the orbital frequency scales as

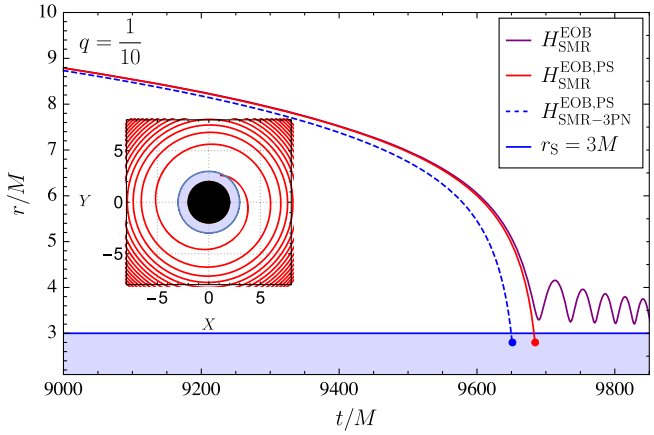

FIG. 1. Plunges through the light-ring radius: the evolved orbital separation for the SMR Hamiltonians is presented. The effective masses of models $H^{\rm EOB,PS}_{\rm SMR}$ and $H^{\rm EOB,PS}_{\rm SMR\text{-}3PN}$ plunge through the LR radius $r_S = 3M$. Conversely, the plunge of the effective mass of $H^{\rm EOB}_{\rm SMR}$ presents unphysical features associated to the LR divergence.

[5]Here $D(\hat{r})$ is the inverse of $\bar{D}(\hat{r})$ mentioned in Sec. II.

[6]The effective Hamiltonian in the PS gauge (2.7) is obtained solving the Hamilton-Jacobi equations with the Schwarzschild metric. The $A(\hat{r})$ and $D(\hat{r})$ are therefore fixed by their Schwarzschild limits.

$$\Omega = \frac{\partial H_{\rm EOB}}{dp_\phi} \propto \frac{\partial H^{\rm PS}_{\rm eff}}{\partial p_\phi} \propto \frac{\partial H^{\rm PS}_{\rm eff}}{\partial H_{\rm S}} \frac{\partial H_{\rm S}}{\partial p_\phi}, \tag{4.5}$$

where in the first proportionality relation we have used the energy map (2.1) and in the second we have exploited the fact that the PS effective Hamiltonian only depends on the angular momentum p_ϕ via $H_{\rm S}$. The factor $\partial H_{\rm S}/\partial p_\phi$ vanishes at $u = 1/2$ (corresponding to the usual Schwarzschild horizon). However, we also find that, with our Hamiltonian ansatz, the $\partial \hat{H}^{\rm PS}_{\rm eff}/\partial H_{\rm S}$ factor develops a zero just below the LR radius. Consequently, Ω vanishes at this point and we stop the evolution. We note that having little model dynamics after the peak of the frequency, while not presenting an issue by itself, could pose problems in the modeling of EOB waveforms and frequencies during the transition between plunge and merger-ringdown phases.

B. Comparisons against numerical relativity

Here we study the energetics of the $H^{\rm EOB,PS}_{\rm SMR}$ and $H^{\rm EOB,PS}_{\rm SMR\text{-}3PN}$ models and the PN EOB models in both gauges via comparisons of their binding energies against NR predictions. The main reason why we choose to compare SMR models to PN ones is to assess how useful SMR information could be in improving the EOB models currently in use, which are based on PN information.

The (quasi) gauge-invariant relations between the dimensionless circular-orbit binding energy $E \equiv (H - M)/\mu$ and angular momentum $l \equiv \hat{p}_\phi = p_\phi/(M\mu)$ (and orbital frequency $\hat{\Omega}$) are used to draw comparisons against NR. This type of comparison is useful to understand how information of the real two-body motion is resummed into the conservative dynamics [51]. In contrast to Ref. [51] and Sec. III of this paper, where the binding energy is calculated in the circular-orbit limit, the binding energies appearing in this section are obtained evolving the EOB Hamiltonians along quasicircular orbits. This more closely matches the procedure used to extract the binding energy from NR simulations of quasicircular inspirals, providing clearer comparisons [106]. Finally, we calculate the dephasing $\Delta\phi_{22} \equiv \phi_{\rm NR} - \phi_{\rm EOB}$ of the $(\ell, m) = (2, 2)$ modes of the $H^{\rm EOB,PS}_{\rm SMR}$ and $H^{\rm EOB,PS}_{\rm SMR\text{-}3PN}$ models against NR results. While more thorough comparisons aimed at using the models for LIGO inference studies would need a systematic calculation of the unfaithfulness (see e.g., Refs. [12,14–16]), we find these comparisons illustrative to contextualize the $H^{\rm EOB,PS}_{\rm SMR}$ and $H^{\rm EOB,PS}_{\rm SMR\text{-}3PN}$ models in this paper.

We employ a set of ten nonspinning NR simulations from the Simulating eXtreme Spacetimes (SXS) Collaboration [4,107], with mass ratios $1/10 \leq q \leq 1$. We summarize the details of these simulations in Table II. A description of how the $E(l)$ and $E(\hat{\Omega})$ curves were calculated for a subset of these simulations can be found in Ref. [106].

We evolve EOB Hamiltonians with PN information up to third order, since 3PN is the order at which PS-gauge Hamiltonians can be uniquely derived for generic orbits (see the Appendix of Ref. [51] for more details). It is worthwhile to mention that the $H^{\rm EOB}_{\rm 3PN}$ Hamiltonian has better energetics and phases performances against NR than both $H^{\rm EOB}_{\rm 4PN}$ and the SEOBNR Hamiltonian used as a baseline for the current generation of EOB waveform models (defined, e.g., in the Appendix of Ref. [102]), when calibration and NQC parameters are turned off. Restricting ourselves to comparisons with $H^{\rm EOB}_{\rm 3PN}$ only, we are therefore not running the risk to overestimate the performance of SMR models when comparing them to PN results.

TABLE II. Set of nonspinning NR simulations and alignment time windows. We list the SXS IDs, the mass ratios q and the number of orbital cycles $N^{\rm merg}_{\rm orb}$ from the beginning of the simulation up to the binary-black-hole merger (peak of $h^{\rm NR}_{22}$), as reported in the SXS catalog. We further include the time $t^{\rm alig}_{\rm in}$ at which the alignment procedure starts, the time $t^{\rm alig}_{\rm fin}$ at which it ends (in units of M) and the estimated NR error at merger $\Delta\phi^{\rm merg}_{\rm NR}$ (in radians).

SXS ID:	q^{-1}	$N^{\rm merg}_{\rm orb}$	$t^{\rm alig}_{\rm in}$	$t^{\rm alig}_{\rm fin}$	$\Delta\phi^{\rm merg}_{\rm NR}$
0180	1	28.18	820	2250	±0.25
1222	2	28.76	1000	2555	±1.26
1221	3	27.18	1800	3000	±0.21
1220	4	26.26	1800	3000	±1.82
0056	5	28.81	1500	3000	±0.39
0181	6	26.47	1000	2500	±0.01
0298	7	19.68	780	2180	±0.10
0063	8	25.83	1140	2540	±0.85
0301	9	18.93	780	2180	±0.13
0303	10	19.27	700	1900	±0.49

Let us begin comparing the $E(l)$ and $E(\hat{\Omega})$ curves. In Figs. 2 and 3, the difference $\Delta E \equiv |E_{\rm NR} - E_{\rm EOB}|$ is plotted for a variety of EOB models and for mass ratios $q = 1$ and $q = 1/10$. We choose to present results for these mass ratios only as we find them to be representative of the behavior of the models across the parameter range considered in this study. Considering the $E(l)$ relations first and focusing on the SMR models, it is seen that for $q = 1/10$ both $H^{\rm EOB,PS}_{\rm SMR}$ and $H^{\rm EOB,PS}_{\rm SMR\text{-}3PN}$ perform better against NR than the 3PN model in the same gauge, e.g., $H^{\rm EOB,PS}_{\rm 3PN}$. The $H^{\rm EOB,PS}_{\rm SMR\text{-}3PN}$ model also performs better than both in the comparable-mass case. A similar finding is obtained investigating the $E(\hat{\Omega})$ curves, see Fig. 3. Taken together, these results highlight the importance of SMR results to improve the modeling of both equal- and unequal-mass systems within the EOB approach. It is also seen that, for both mass ratios considered and for both $E(l)$ and $E(\hat{\Omega})$ curves, $H^{\rm EOB,PS}_{\rm SMR\text{-}3PN}$ improves the predictions of $H^{\rm EOB,PS}_{\rm SMR}$, suggesting that generic-orbit terms are important when considering quasicircular-orbit binding energies (especially in the equal-mass-ratio case).

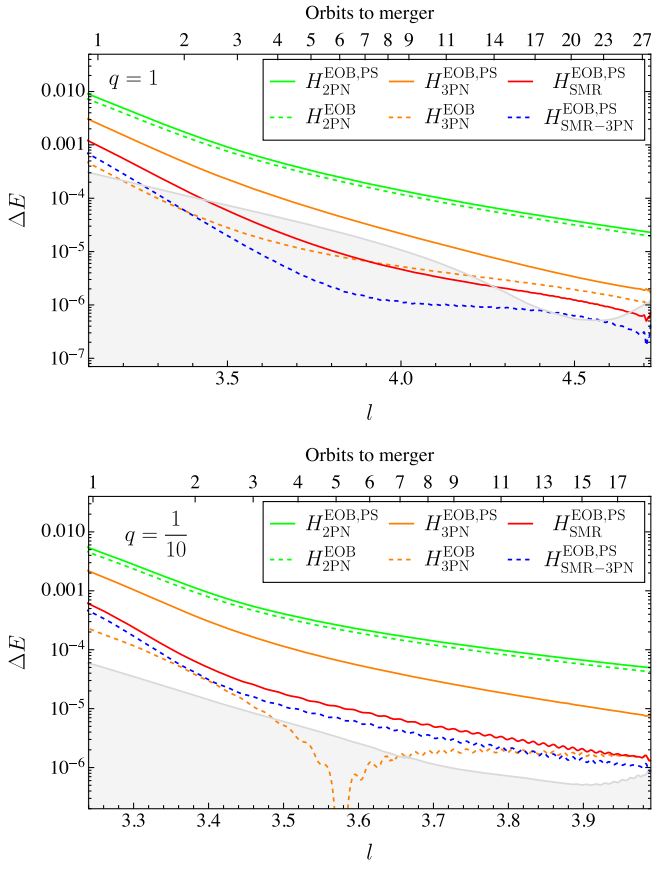

FIG. 2. SMR vs PN binding energies: we compare the difference ΔE in binding energy from NR for our SMR Hamiltonians versus angular momentum l. We compare it to similar results for PN models up to third order, in both PS and DJS gauges. The *estimated* NR error is shown in grey.

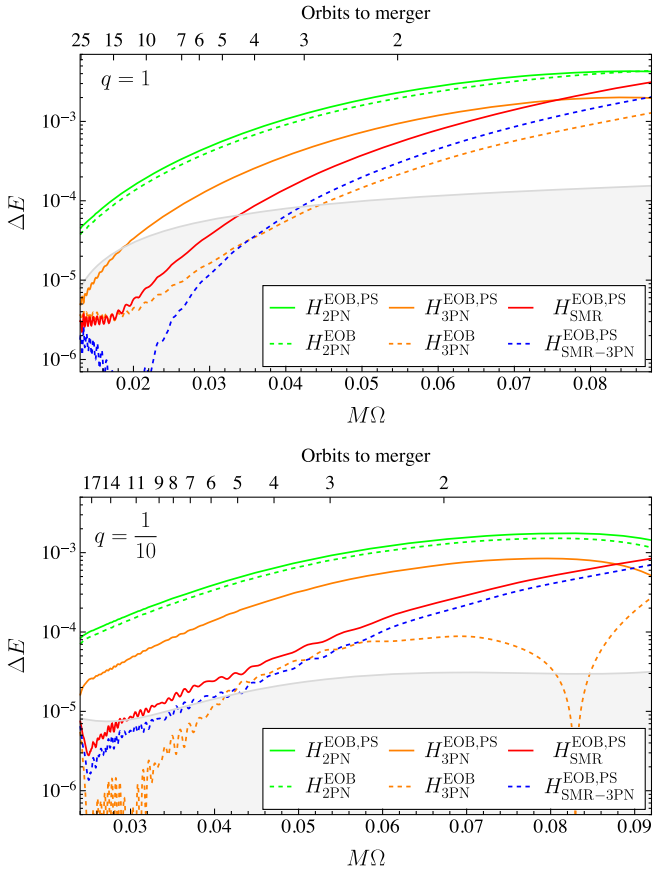

FIG. 3. SMR vs PN binding energies: we compare the difference ΔE in binding energy from NR for our SMR Hamiltonians versus frequency ($M\Omega$). We compare it to similar results for PN models up to third order, in both PS and DJS gauges. The *estimated* NR error is shown in grey.

PN Hamiltonians in the PS gauge generically perform worse in binding energy comparisons than Hamiltonians in the DJS gauge, as found out in the adiabatic approximation already in Ref. [51]. This finding suggests that, notwithstanding the already good agreement between SMR models and NR simulations for both mass ratios, a better description for the EOB dynamics than the one provided by the PS gauge could be pursued in order to maximize the performance of evolutions from both PN and SMR EOB models.

We complete our comparison study with the dephasing $\Delta\phi_{22}$ of the $(\ell, m) = (2, 2)$ modes from the EOB models and the NR simulations. For a proper comparison, the EOB and NR waveforms must be aligned for each q. Here we use the alignment procedure outlined in Ref. [12], which amounts to minimizing the function:

$$\Xi(\Delta t, \Delta\phi) = \int_{t_1^{\rm alig}}^{t_2^{\rm alig}} [\phi_{\rm NR}(t) - \phi_{\rm EOB}(t + \Delta t) - \Delta\phi]^2 dt, \tag{4.6}$$

over the time and phase shifts, Δt and $\Delta\phi$. The integrating interval $[t_1^{\rm alig}, t_2^{\rm alig}]$ defines the time-domain window in which the alignment is performed: conservatively, it must be chosen in the inspiral of the NR simulation, large enough to average out the numerical noise and such as to avoid junk radiation at the beginning of the NR simulation [12]. From the alignment procedure described above, one can obtain the phase and amplitude time shift to be applied to the EOB model to align it with the NR waveforms, i.e., the aligned waveforms are

$$h_{22}^{\rm NR} = A_{\rm NR}(t) e^{i\phi_{\rm NR}(t)}, \tag{4.7}$$

$$h_{22}^{\rm EOB} = A_{\rm EOB}(t + \Delta t) e^{i[\phi_{\rm EOB}(t+\Delta t)+\Delta\phi]}. \tag{4.8}$$

Our choices for the time windows are reported in Table II. In Fig. 4, we show the results of our phase comparisons for $q = 1$ and $q = 1/10$ up to merger. For clarity, the upper panels only include the $H^{\rm EOB,PS}_{\rm SMR}$ and $H^{\rm EOB,PS}_{\rm SMR\text{-}3PN}$ models and the NR simulations. They show the real parts of Eqs. (4.7) and (4.8), from which we infer that

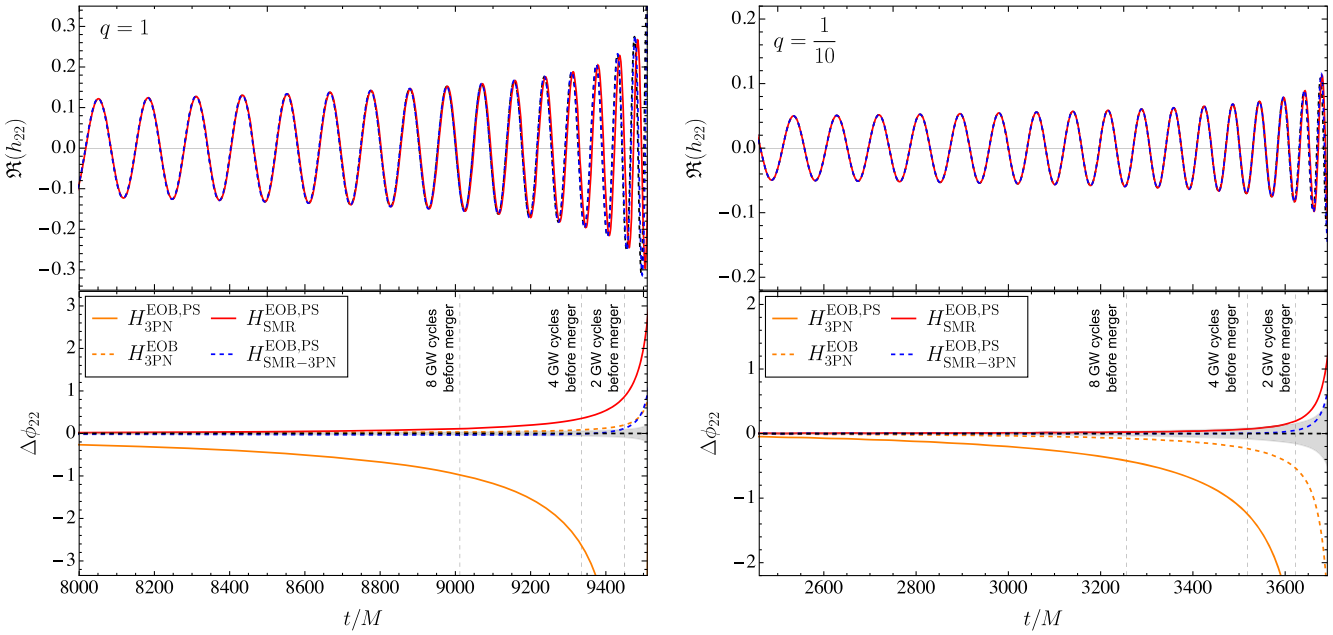

FIG. 4. Dephasing of EOB models: in the top panels, the real parts $\Re(h_{22})$ of the $(\ell, m) = (2, 2)$ mode EOB waveform for the SMR, SMR-3PN models are shown and compared to the NR waveforms (in dashed-black, overlapping with the EOB waveforms up to few GW cycles to merger). In the lower panels, the dephasing of SMR and PN EOB models from the NR simulations is calculated. Also shown are the times corresponding to 8, 4 and 2 GW cycles before NR merger.

the SMR models do not accumulate a significant amount of dephasing. Overall, they are in very good agreement with NR for both $q = 1$ and $q = 1/10$. It is important to place the above results in context. In the lower panel, the dephasing of SMR models from NR is compared to that of 3PN models.[7] Interestingly, even in the equal-mass-ratio case $H^{\rm EOB,PS}_{\rm SMR}$ and $H^{\rm EOB,PS}_{\rm SMR\text{-}3PN}$ compare much better than the 3PN model in the same gauge, e.g., $H^{\rm EOB,PS}_{\rm 3PN}$. Their dephasing is comparable to $H^{\rm EOB}_{\rm 3PN}$. In the $q = 1/10$ case, they have a smaller dephasing than any other PN model considered in this study. In Table III, we report the dephasing that the $H^{\rm EOB,PS}_{\rm SMR}$, $H^{\rm EOB,PS}_{\rm SMR\text{-}3PN}$, $H^{\rm EOB}_{\rm 3PN}$ and $H^{\rm EOB,PS}_{\rm 3PN}$ models accumulate up to 8 and 4 GW cycles before merger for all mass ratios (with the corresponding estimated NR error).[8]

Next, we want to study how the dephasing of the above models varies as a function of q. It would be tempting to compare the $\Delta\phi$'s reported in Table III at a fixed number of cycles before merger. While this remains a valid possibility, such a comparison would neither take into account the different lengths of the NR simulations used in this set, nor the different number of GW cycles encompassed by the time windows of Table II. To keep both parameters under control, we realign our models with alternative time windows that are dictated by the number of GW cycles to merger $\Delta N_{\rm GW}(t) \equiv N_{\rm GW}(t) - N^{\rm merg}_{\rm GW}$ of the NR simulations. That is, for each mass ratio we fix a different time window $[t^{\rm alig}_1, t^{\rm alig}_2]$, corresponding to the *same* interval of cycles to merger $[\Delta N_{\rm GW}(t^{\rm alig}_1), \Delta N_{\rm GW}(t^{\rm alig}_2)]$. The benefits of this choice are twofold. To begin with, the alignment windows thus calculated depends on the position of the NR merger (peak of $h^{\rm NR}_{22}$), which is a quantifiable feature of every NR simulation. Moreover, this choice allows us to assess trends across the mass ratios fairly, since the waveforms thus aligned are compared in the same range of GW cycles. A caveat for this alignment method is that the GW cycles of evolutions with smaller q lie in a regime of stronger gravity.

We choose to align the EOB models to NR in an interval of $N_{\rm GW}$ such that $[\Delta N_{\rm GW}(t^{\rm alig}_1), \Delta N_{\rm GW}(t^{\rm alig}_2)] = [-34, -24]$, corresponding to the time-windows reported in Table IV. This choice stems from the length of the shortest NR simulation, e.g., $q = 1/9$, which counts $N^{\rm merg}_{\rm GW} = 37.86$ GW cycles at merger (the first $\sim$3 GW cycles of this simulation are neglected in order to avoid junk radiation). In Fig. 5, we plot the dephasing for the three models that perform best in Fig. 4: that is, $H^{\rm EOB}_{\rm 3PN}$, $H^{\rm EOB,PS}_{\rm SMR}$ and $H^{\rm EOB,PS}_{\rm SMR\text{-}3PN}$ and study the trends across q. For every simulation, we calculate the dephasing 8 and 4 GW cycles before merger to show the robustness of

[7]In this comparison we do not include 2PN models, which we find to have much larger dephasing than the 3PN models shown.

[8]We have checked that shifting the time windows by $\Delta t = \pm 100M$, our $\Delta\phi$'s only change by a few hundredths of a radian.

TABLE III. Details of the dephasing comparison. We report the dephasing (in radians) of the SMR and 3PN models in both gauges at 8 and 4 GW cycles before NR merger, as found using the time windows of Table II. We also report the corresponding estimated NR error, which we denote by $\Delta\phi_{\rm NR}$. The error for each NR simulation is estimated taking the phase differences between the highest two resolutions of the NR simulation (at fixed extrapolation order) and between two successive extrapolation orders (at fixed resolution), and adding them in quadrature.

	8 GW Cycles before merger					4 GW Cycles before merger				
q^{-1}	$\Delta\phi^{\rm EOB,PS}_{\rm SMR}$	$\Delta\phi^{\rm EOB,PS}_{\rm SMR\text{-}3PN}$	$\Delta\phi^{\rm EOB,PS}_{\rm 3PN}$	$\Delta\phi^{\rm EOB}_{\rm 3PN}$	$\Delta\phi_{\rm NR}$	$\Delta\phi^{\rm EOB,PS}_{\rm SMR}$	$\Delta\phi^{\rm EOB,PS}_{\rm SMR\text{-}3PN}$	$\Delta\phi^{\rm EOB,PS}_{\rm 3PN}$	$\Delta\phi^{\rm EOB}_{\rm 3PN}$	$\Delta\phi_{\rm NR}$
1	0.111	−0.033	−0.971	0.032	±0.032	0.352	−0.012	−2.630	0.084	±0.056
2	0.112	−0.061	−1.342	−0.023	±0.105	0.512	−0.021	−5.586	−0.043	±0.224
3	0.050	−0.021	−0.617	−0.023	±0.093	0.111	−0.026	−1.209	−0.048	±0.144
4	0.046	−0.038	−0.859	−0.078	±0.203	0.187	−0.041	−2.540	−0.212	±0.372
5	0.037	−0.034	−0.846	−0.086	±0.023	0.125	−0.044	−2.077	−0.211	±0.064
6	−0.035	−0.064	−0.433	−0.093	±0.006	−0.041	−0.082	−0.599	−0.126	±0.007
7	0.024	−0.009	−0.462	−0.070	±0.001	0.092	−0.003	−1.403	−0.211	±0.009
8	0.021	−0.021	−0.676	−0.107	±0.057	0.076	−0.025	−1.660	−0.260	±0.155
9	0.017	−0.005	−0.368	−0.068	±0.002	0.063	−0.005	−1.185	−0.220	±0.012
10	0.022	−0.001	−0.413	−0.076	±0.033	0.070	−0.004	−1.245	−0.233	±0.083

TABLE IV. Alternative alignment time windows. Time windows (in units of M) employed for Fig. 5: here, $t^{\rm alig}_{\rm in}$ is the time corresponding to 34 GW cycles before merger for each NR simulation, whereas $t^{\rm alig}_{\rm fin}$ is chosen to encompass 10 GW cycles. The time at merger is given by $t_{\rm merg}$.

q^{-1}	$t^{\rm alig}_{\rm in}$	$t^{\rm alig}_{\rm fin}$	$t_{\rm merg}$	q^{-1}	$t^{\rm alig}_{\rm in}$	$t^{\rm alig}_{\rm fin}$	$t_{\rm merg}$
1	5107	6911	9517	6	2971	4254	6000
2	5406	7078	9384	7	776	2083	4142
3	3940	5532	7858	8	2652	3918	5956
4	3479	4975	7200	9	513	1732	3692
5	4206	5641	7864	10	587	1771	3691

the trends.[9] Noticeably, the 3PN EOB waveform in the DJS gauge starts degrading in accuracy as the mass ratio is decreased, while the SMR and SMR-3PN ones improve: remarkably, for most q's, the SMR-3PN model only dephases by a few hundredths of a radian up to 4 GW cycles before merger. Moreover, we notice that SMR models start performing better than $H^{\rm EOB}_{\rm 3PN}$ for $q \lesssim 1/3$, hinting again to the fact that SMR information, when reorganized in the EOB framework, could be used to model systems that are very close to the equal-mass-ratio regime [66,86].

The picture emerging from Fig. 5 is that the SMR-3PN model is the most consistent of the two models with SMR information, corroborating the findings for $q = 1$ and $q = 1/10$ in the binding energy comparisons. The small dephasing of the SMR-3PN model suggests that the Hamiltonian upon which it is based is a possible starting point to develop a new generation of EOB waveform models able to tackle the currently challenging intermediate-mass-ratio regime.

[9]We have also checked that the trends are unaffected by variations in the number of orbital cycles in the alignment window.

V. DISCUSSION AND CONCLUSIONS

The complete EOB Hamiltonian at linear order in SMR from Ref. [85] suffers from a coordinate singularity at the LR radius in the deformed-Schwarzschild background. Building on Refs. [47,97], we have constructed two Hamiltonians in the PS reformulation of the EOB approach [47,51] (both with the SMR correction to the Detweiler redshift and with mixed SMR-3PN information), and checked that they are not affected by poles at the LR radius (and related unphysical features) by studying plunging trajectories.

We have then explored the merits of the SMR and mixed SMR-3PN Hamiltonians via comparisons of their waveforms and binding energies, and those of PN Hamiltonians in different gauges, against NR predictions. Ultimately, we find that:

(1) For both $q = 1$ and $q = 1/10$, the binding energies of SMR and SMR-3PN EOB models (see Figs. 2 and 3) generally compare better against NR than the binding energy of the PS Hamiltonian with 3PN information.
(2) The generic-orbit 3PN information in the SMR-3PN EOB Hamiltonian improves the binding energy and phase comparisons of SMR EOB models.
(3) PN Hamiltonians in the EOB-PS gauge have binding energies that compare worse than those from PN Hamiltonians in the standard EOB gauge, confirming the findings of Ref. [51] and extending their validity to nonadiabatic evolutions.
(4) The SMR-3PN EOB model agrees remarkably well against NR simulations, see Fig. 5. The dephasing up to 4 GW cycles before merger is a few hundredths of a radian for $q \lesssim 1/3$ and a tenth of a radian for

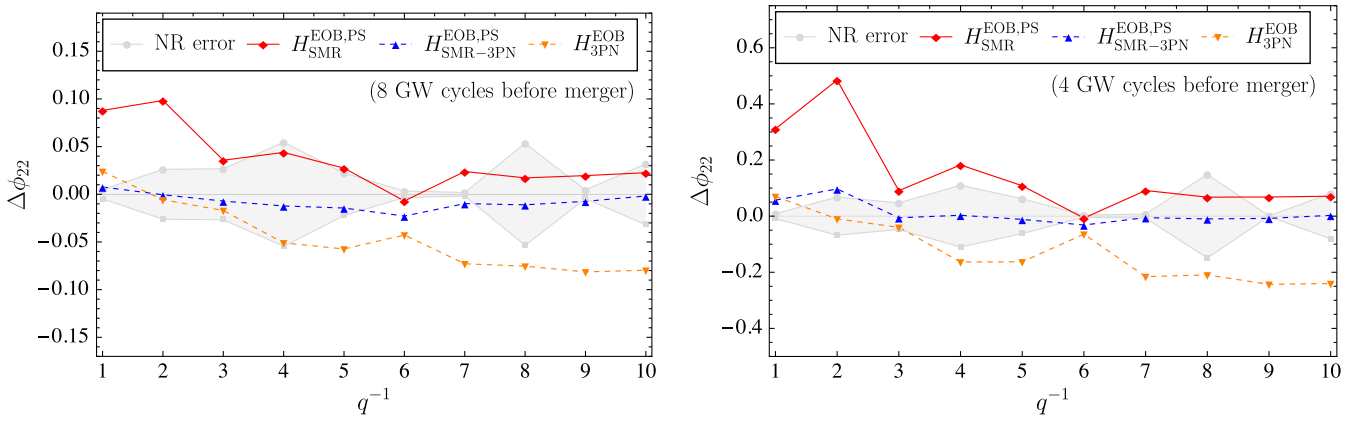

FIG. 5. Dephasing vs mass ratio: we compare the dephasing of $H^{\rm EOB,PS}_{\rm SMR}$, $H^{\rm EOB,PS}_{\rm SMR-PN}$ and $H^{\rm EOB}_{\rm 3PN}$ after they have been aligned with the NR simulations from Table IV. For each q, we snapshot the dephasing of the EOB models and the NR simulation at a time corresponding to 4 and 2 orbits before the merger of the binary system in the NR simulation.

$q > 1/3$. The only EOB PN model with comparable dephasing is the 3PN EOB Hamiltonian in the DJS gauge for $q \gtrsim 1/3$.

The construction of the SMR EOB Hamiltonian in this paper depends on a number of choices. First of all, we chose to fix the coordinate freedom in the effective Hamiltonian using the PS gauge. This was chosen because of its relative simplicity, while allowing a natural path towards avoiding singularities at the light ring. However, there may exist different choices that are equally (or more) effective. Second, while the EOB Hamiltonian in principle applies to generic orbits, we fix the linear-in-ν part only by comparing to the circular-orbit binding energy. Consequently, there is considerable freedom in the "non-circular-orbit" part of the Hamiltonian. In practice, we fix this freedom by choosing the specific functional dependence of the effective Hamiltonian on $\hat{H}_{\rm S}$ given by Eq. (3.5). This choice is in part restricted by the requirement that the Hamiltonian be analytic, but other options are available. Third and finally, SMR data for the binding energy extends only to the light ring. The Hamiltonian in the region $u > \frac{1}{3}$ therefore depends only on the analytic extension of the redshift data. Given that this data is known only to finite numerical precision, there is some freedom in the choice of the exact analytical form of its fit. This choice can also affect the relative size of the different coefficient functions in Eq. (3.5).

Our investigation opens up further avenues of research. To begin with, one can study whether it is possible to uniquely fix other EOB gauges that could accommodate the Detweiler redshift (without introducing a LR divergence) and study their merits via comparisons against NR. As discussed already in Ref. [97], to solve the LR divergence arising in this context the nongeodesic function $\hat{Q}$ needs a term proportional to p^3_ϕ, possibly resummed in another quantity (as done in the PS gauge using $\hat{H}_{\rm S}$). It would be quite interesting to see whether other gauges that allow solving the LR divergence also improve the comparisons against NR predictions. One concrete example of different resummation that was shown to improve the comparisons of the conservative sector of post-Minkowskian Hamiltonians in PS form has been given in the Appendix of Ref. [51]. It is worthwhile to study whether a similar choice could work for the SMR and SMR-3PN models herein presented. The hope is that using different resummations, and including information from the second order in the SMR, one could obtain a considerably improved EOB Hamiltonian that, after further calibration to NR, would be very useful for LIGO/Virgo analyses in the near future.

Further research endeavors could be directed towards informing the EOB with different SMR quantities than the circular-orbit Detweiler redshift. An example of a quantity that still needs to be fully exploited is the generalized redshift [77,78], which includes information for arbitrarily eccentric orbits. We envision using EOB Hamiltonians at linear and higher orders in the mass ratio for inference studies in the future detectors' era, when precise models will be needed to properly characterize high signal-to-noise systems, possibly having rather small mass ratios. In order for this program to be achieved, not only should the conservative sector be optimized with both results at second order in q and (potentially) a better resummation, but information from other crucial physical quantities should also be incorporated: notably missing features in our analysis are the spin and eccentricity. Furthermore, a more comprehensive study of the dissipative sector must be pursued. It would be desirable, for instance, to include more self-force information in the flux. Lastly, we would also need to build the full inspiral, merger and ringdown waveforms, and calibrate them to NR simulations. We leave these important investigations to future work.

ACKNOWLEDGMENTS

It is a pleasure to thank Sergei Ossokine for providing us with the NR data used for the comparisons, and Tanja

Hinderer for the original version of the EOB evolution code in *Mathematica* used in this paper. A. A. would like to further thank Sergei Ossokine and Roberto Cotesta for many fruitful discussions over the preparation of this paper. M. v. d. M. was supported by European Union's Horizon 2020 research and innovation programme under Grant agreement No. 705229. This work makes use of the Black Hole Perturbation Toolkit [108].

APPENDIX: DETWEILER-REDSHIFT DATA AND FIT

The linear-in-ν Detweiler redshift Δz at a fixed x is given by Refs. [76,78]:

$$\Delta z = -\frac{1}{2}\sqrt{1-3x}h^{\mathrm{R}}_{uu}(x) + \frac{x}{\sqrt{1-3x}}, \tag{A1}$$

where h^{R}_{uu} is the double contraction of the regular part of the metric perturbation generated by a particle on a circular orbit with its 4-velocity. We determine h^{R}_{uu} in a range $0 < x < 1/3$ to a high precision using the numerical code developed in Ref. [57]. In this code the regular part of the metric perturbation is extracted using the mode-sum formalism. As noted in Ref. [97], the convergence of the mode sum decreases drastically as circular orbits approach the light ring. This limits the accuracy with which h^{R}_{uu} can be obtained. The code from Ref. [57] allows calculations using arbitrary precision arithmetic, which allows us to calculate Δz much closer to the light ring and at much higher precision than previously done in Ref. [97]. For this paper, we have generated data for Δz using up to 120ℓ modes, which allows us to obtain Δz up to $(1-3x) \approx 4\times 10^{-5}$, with relative accuracy $\lesssim 2.5\times 10^{-5}$.

To utilize the Δz data in our SMR EOB model we need an analytic fit to the data. Two aspects of this fit are important to control for the behavior of the model. First, the model is sensitive to the precise analytical structure of the fit near the light ring. Second, we need to control the behavior of the fit beyond the light ring $x > 1/3$, where we have no self-force data. In light of these two considerations, we want to fit the data with a model having a relatively low number of parameters. To achieve this, we leverage the analytic knowledge of the PN expansion of Δz, which Ref. [79] calculated up to 21.5PN order. We construct a fit of the overall form:

$$\Delta z = Z_0(x) + \frac{(1-2x)^5}{1-3x} Z_{\mathrm{PN}}(x)[1+\alpha(x)Z_{\mathrm{fit}}(x)]. \tag{A2}$$

The leading term

$$Z_0(x) = x\frac{1-4x}{1-3x} + \frac{x}{\sqrt{1-3x}}, \tag{A3}$$

is constructed such that it will exactly cancel the coefficients $\tilde{f}_0$ and $\tilde{f}_1$ when matched to the SMR EOB Hamiltonian.

The number of factors $(1-2x)$ in front of the second term has been chosen such that the resulting contribution to the effective Hamiltonian $\hat{Q}^{\mathrm{PS}}_{\mathrm{SMR}}$ vanishes at the horizon of the effective spacetime, $x = 1/2$. The coefficient function, $Z_{\mathrm{PN}}(x)$ has the form:

$$Z_{\mathrm{PN}}(x) = 2x^3 \sum_{i,j} a_{i,j} x^{i/2} \log^j x, \tag{A4}$$

where the coefficients $a_{i,j}$ are obtained by requiring that the series expansion of Eq. (A2) matches the 21.5PN expression from Ref. [79]. Since these coefficients are numerous and lengthy, and are easily obtained using computer algebra and the expressions available for the Black Hole Peturbation Toolkit [108], we do not reproduce them explicitly here.

The actual fit Z_{fit} is multiplied by an attenuation function:

$$\alpha(x) = \exp\left(\frac{4-x^{-2}}{6}\right), \tag{A5}$$

that suppresses the fit exponentially in the weak-field regime, ensuring that the PN behavior of Δz is unaffected by the fit. The function $\alpha(x)$ has been chosen such that $\alpha(1/2) = 1$ and is at its steepest at $x = 1/3$.

The fit Z_{fit} itself is a polynomial in $\beta \equiv 9x(1-3x)(1-2x)$ and $\log[\frac{1-3x}{(1-2x)^2}]$ with arbitrary coefficients. We perform a large number of linear fits for varying combinations of five terms, and compare various "goodness of fit" indicators such as the adjusted R^2 value and Bayesian information criterion. One model that consistently outperformed the others is

$$Z_{\mathrm{fit}} = c_0 + c_1\beta + c_2\beta^4 + (c_3\beta + c_4\beta^4)\log\left[\frac{1-3x}{(1-2x)^2}\right], \tag{A6}$$

with

$$c_0 = 0.555947, \tag{A7a}$$

$$c_1 = -2.589868, \tag{A7b}$$

$$c_2 = 31.144986, \tag{A7c}$$

$$c_3 = 2.440115, \tag{A7d}$$

$$c_4 = -179.175818. \tag{A7e}$$

With this fit the coefficient functions f_i in Eq. (3.5) become

$$f_0(x) = (1-3x)Z_{\rm PN}(x)[1+\alpha(x)(c_0+c_1\beta+c_2\beta^4)], \tag{A8}$$

$$f_1(x) = 0, \tag{A9}$$

$$f_2(x) = (1-2x)^2 Z_{\rm PN}(x)[1+\alpha(x)(c_3\beta+c_4\beta^4)]. \tag{A10}$$

[1] F. Pretorius, Phys. Rev. Lett. **95**, 121101 (2005).
[2] M. Campanelli, C. O. Lousto, P. Marronetti, and Y. Zlochower, Phys. Rev. Lett. **96**, 111101 (2006).
[3] J. G. Baker, J. Centrella, D.-I. Choi, M. Koppitz, and J. van Meter, Phys. Rev. Lett. **96**, 111102 (2006).
[4] A. H. Mroue *et al.*, Phys. Rev. Lett. **111**, 241104 (2013).
[5] K. Jani, J. Healy, J. A. Clark, L. London, P. Laguna, and D. Shoemaker, Classical Quantum Gravity **33**, 204001 (2016).
[6] J. Healy, C. O. Lousto, Y. Zlochower, and M. Campanelli, Classical Quantum Gravity **34**, 224001 (2017).
[7] T. Dietrich, D. Radice, S. Bernuzzi, F. Zappa, A. Perego, B. Brügmann, S. V. Chaurasia, R. Dudi, W. Tichy, and M. Ujevic, Classical Quantum Gravity **35**, 24LT01 (2018).
[8] M. Boyle *et al.*, Classical Quantum Gravity **36**, 195006 (2019).
[9] L. Blanchet, Living Rev. Relativity **17**, 2 (2014).
[10] L. Barack and A. Pound, Rep. Prog. Phys. **82**, 016904 (2019).
[11] A. Le Tiec, Int. J. Mod. Phys. D **23**, 1430022 (2014).
[12] Y. Pan, A. Buonanno, M. Boyle, L. T. Buchman, L. E. Kidder, H. P. Pfeiffer, and M. A. Scheel, Phys. Rev. D **84**, 124052 (2011).
[13] A. Taracchini, Y. Pan, A. Buonanno, E. Barausse, M. Boyle, T. Chu, G. Lovelace, H. P. Pfeiffer, and M. A. Scheel, Phys. Rev. D **86**, 024011 (2012).
[14] A. Taracchini *et al.*, Phys. Rev. D **89**, 061502 (2014).
[15] A. Bohé *et al.*, Phys. Rev. D **95**, 044028 (2017).
[16] R. Cotesta, A. Buonanno, A. Bohé, A. Taracchini, I. Hinder, and S. Ossokine, Phys. Rev. D **98**, 084028 (2018).
[17] B. P. Abbott *et al.* (Virgo and LIGO Scientific Collaborations), Phys. Rev. Lett. **116**, 061102 (2016).
[18] B. P. Abbott *et al.* (Virgo and LIGO Scientific Collaborations), Phys. Rev. Lett. **116**, 241103 (2016).
[19] B. P. Abbott *et al.* (Virgo and LIGO Scientific Collaborations), Phys. Rev. Lett. **118**, 221101 (2017); **121**, 129901(E) (2018).
[20] B. P. Abbott *et al.* (Virgo and LIGO Scientific Collaborations), Phys. Rev. Lett. **119**, 141101 (2017).
[21] B. P. Abbott *et al.* (Virgo and LIGO Scientific Collaborations), Astrophys. J. **851**, L35 (2017).
[22] B. P. Abbott *et al.* (Virgo and LIGO Scientific Collaborations), Phys. Rev. Lett. **119**, 161101 (2017).
[23] B. P. Abbott *et al.* (LIGO Scientific and Virgo Collaborations), Phys. Rev. X **9**, 031040 (2019).
[24] B. P. Abbott *et al.* (Virgo and LIGO Scientific Collaborations), Phys. Rev. Lett. **116**, 241102 (2016).
[25] B. P. Abbott *et al.* (Virgo and LIGO Scientific Collaborations), Phys. Rev. Lett. **116**, 221101 (2016).
[26] H. Audley *et al.* (LISA Collaboration), arXiv:1702.00786.
[27] M. Punturo *et al.*, Classical Quantum Gravity **27**, 194002 (2010).
[28] B. P. Abbott *et al.* (LIGO Scientific Collaboration), Classical Quantum Gravity **34**, 044001 (2017).
[29] A. Buonanno and T. Damour, Phys. Rev. D **59**, 084006 (1999).
[30] A. Buonanno and T. Damour, Phys. Rev. D **62**, 064015 (2000).
[31] T. Damour, P. Jaranowski, and G. Schäfer, Phys. Rev. D **62**, 084011 (2000).
[32] P. Jaranowski and G. Schäfer, Phys. Rev. D **92**, 124043 (2015).
[33] T. Damour, P. Jaranowski, and G. Schäfer, Phys. Rev. D **89**, 064058 (2014).
[34] T. Damour, P. Jaranowski, and G. Schäfer, Phys. Rev. D **93**, 084014 (2016).
[35] L. Bernard, L. Blanchet, A. Bohé, G. Faye, and S. Marsat, Phys. Rev. D **93**, 084037 (2016).
[36] L. Bernard, L. Blanchet, A. Bohé, G. Faye, and S. Marsat, Phys. Rev. D **95**, 044026 (2017).
[37] L. Bernard, L. Blanchet, A. Bohé, G. Faye, and S. Marsat, Phys. Rev. D **96**, 104043 (2017).
[38] S. Foffa and R. Sturani, Phys. Rev. D **100**, 024047 (2019).
[39] S. Foffa, R. A. Porto, I. Rothstein, and R. Sturani, Phys. Rev. D **100**, 024048 (2019).
[40] S. Foffa, P. Mastrolia, R. Sturani, C. Sturm, and W. J. Torres Bobadilla, Phys. Rev. Lett. **122**, 241605 (2019).
[41] J. Blümlein, A. Maier, and P. Marquard, Phys. Lett. B **800**, 135100 (2020).
[42] T. Damour, P. Jaranowski, and G. Schäfer, Phys. Rev. D **91**, 084024 (2015).
[43] T. Damour, B. R. Iyer, and A. Nagar, Phys. Rev. D **79**, 064004 (2009).
[44] T. Damour and A. Nagar, Phys. Rev. D **79**, 081503 (2009).
[45] E. Barausse and A. Buonanno, Phys. Rev. D **81**, 084024 (2010).
[46] T. Hinderer *et al.*, Phys. Rev. Lett. **116**, 181101 (2016).
[47] T. Damour, Phys. Rev. D **97**, 044038 (2018).
[48] T. Damour, Phys. Rev. D **94**, 104015 (2016).
[49] J. Vines, Classical Quantum Gravity **35**, 084002 (2018).
[50] J. Vines, J. Steinhoff, and A. Buonanno, Phys. Rev. D **99**, 064054 (2019).
[51] A. Antonelli, A. Buonanno, J. Steinhoff, M. van de Meent, and J. Vines, Phys. Rev. D **99**, 104004 (2019).

[52] Y. Mino, M. Sasaki, and T. Tanaka, Phys. Rev. D **55**, 3457 (1997).
[53] T. C. Quinn and R. M. Wald, Phys. Rev. D **56**, 3381 (1997).
[54] L. Barack and N. Sago, Phys. Rev. D **75**, 064021 (2007).
[55] L. Barack and N. Sago, Phys. Rev. D **81**, 084021 (2010).
[56] A. G. Shah, J. L. Friedman, and T. S. Keidl, Phys. Rev. D **86**, 084059 (2012).
[57] M. van de Meent and A. G. Shah, Phys. Rev. D **92**, 064025 (2015).
[58] M. van de Meent, Phys. Rev. D **94**, 044034 (2016).
[59] M. van de Meent, Phys. Rev. D **97**, 104033 (2018).
[60] N. Warburton, S. Akcay, L. Barack, J. R. Gair, and N. Sago, Phys. Rev. D **85**, 061501 (2012).
[61] T. Osburn, N. Warburton, and C. R. Evans, Phys. Rev. D **93**, 064024 (2016).
[62] M. van de Meent and N. Warburton, Classical Quantum Gravity **35**, 144003 (2018).
[63] T. Hinderer and E. E. Flanagan, Phys. Rev. D **78**, 064028 (2008).
[64] L. Barack and N. Sago, Phys. Rev. Lett. **102**, 191101 (2009).
[65] L. Barack, T. Damour, and N. Sago, Phys. Rev. D **82**, 084036 (2010).
[66] A. Le Tiec, A. H. Mroue, L. Barack, A. Buonanno, H. P. Pfeiffer, N. Sago, and A. Taracchini, Phys. Rev. Lett. **107**, 141101 (2011).
[67] M. van de Meent, Phys. Rev. Lett. **118**, 011101 (2017).
[68] S. Akcay, D. Dempsey, and S. R. Dolan, Classical Quantum Gravity **34**, 084001 (2017).
[69] S. Akcay, Phys. Rev. D **96**, 044024 (2017).
[70] S. R. Dolan, N. Warburton, A. I. Harte, A. Le Tiec, B. Wardell, and L. Barack, Phys. Rev. D **89**, 064011 (2014).
[71] C. Kavanagh, D. Bini, T. Damour, S. Hopper, A. C. Ottewill, and B. Wardell, Phys. Rev. D **96**, 064012 (2017).
[72] D. Bini and T. Damour, Phys. Rev. D **90**, 024039 (2014).
[73] D. Bini, T. Damour, A. Geralico, C. Kavanagh, and M. van de Meent, Phys. Rev. D **98**, 104062 (2018).
[74] S. R. Dolan, P. Nolan, A. C. Ottewill, N. Warburton, and B. Wardell, Phys. Rev. D **91**, 023009 (2015).
[75] D. Bini and T. Damour, Phys. Rev. D **90**, 124037 (2014).
[76] S. L. Detweiler, Phys. Rev. D **77**, 124026 (2008).
[77] L. Barack and N. Sago, Phys. Rev. D **83**, 084023 (2011).
[78] S. Akcay, A. Le Tiec, L. Barack, N. Sago, and N. Warburton, Phys. Rev. D **91**, 124014 (2015).
[79] C. Kavanagh, A. C. Ottewill, and B. Wardell, Phys. Rev. D **92**, 084025 (2015).
[80] A. G. Shah, J. L. Friedman, and B. F. Whiting, Phys. Rev. D **89**, 064042 (2014).
[81] N. K. Johnson-McDaniel, A. G. Shah, and B. F. Whiting, Phys. Rev. D **92**, 044007 (2015).
[82] A. Zimmerman, A. G. M. Lewis, and H. P. Pfeiffer, Phys. Rev. Lett. **117**, 191101 (2016).
[83] A. Le Tiec, L. Blanchet, and B. F. Whiting, Phys. Rev. D **85**, 064039 (2012).
[84] T. Damour, Phys. Rev. D **81**, 024017 (2010).
[85] A. Le Tiec, E. Barausse, and A. Buonanno, Phys. Rev. Lett. **108**, 131103 (2012).
[86] E. Barausse, A. Buonanno, and A. Le Tiec, Phys. Rev. D **85**, 064010 (2012).
[87] C. Kavanagh, A. C. Ottewill, and B. Wardell, Phys. Rev. D **92**, 024017 (2015).
[88] S. Hopper, C. Kavanagh, and A. C. Ottewill, Phys. Rev. D **93**, 044010 (2016).
[89] C. Kavanagh, A. C. Ottewill, and B. Wardell, Phys. Rev. D **93**, 124038 (2016).
[90] D. Bini and T. Damour, Phys. Rev. D **89**, 064063 (2014).
[91] D. Bini and T. Damour, Phys. Rev. D **89**, 104047 (2014).
[92] D. Bini and T. Damour, Phys. Rev. D **91**, 064050 (2015).
[93] D. Bini, T. Damour, and A. Geralico, Phys. Rev. D **93**, 064023 (2016).
[94] D. Bini, T. Damour, and A. Geralico, Phys. Rev. D **92**, 124058 (2015); **93**, 109902(E) (2016).
[95] D. Bini, T. Damour, and A. Geralico, Phys. Rev. D **93**, 124058 (2016).
[96] D. Bini, T. Damour, and A. Geralico, Phys. Rev. D **93**, 104017 (2016).
[97] S. Akcay, L. Barack, T. Damour, and N. Sago, Phys. Rev. D **86**, 104041 (2012).
[98] T. Damour, B. R. Iyer, P. Jaranowski, and B. S. Sathyaprakash, Phys. Rev. D **67**, 064028 (2003).
[99] A. Buonanno, Y. Pan, J. G. Baker, J. Centrella, B. J. Kelly, S. T. McWilliams, and J. R. van Meter, Phys. Rev. D **76**, 104049 (2007).
[100] S. Akcay and M. van de Meent, Phys. Rev. D **93**, 064063 (2016).
[101] D. Bini, T. Damour, and G. Faye, Phys. Rev. D **85**, 124034 (2012).
[102] J. Steinhoff, T. Hinderer, A. Buonanno, and A. Taracchini, Phys. Rev. D **94**, 104028 (2016).
[103] A. Le Tiec, Phys. Rev. D **92**, 084021 (2015).
[104] T. Damour and A. Nagar, Phys. Rev. D **76**, 064028 (2007).
[105] Y. Pan, A. Buonanno, R. Fujita, E. Racine, and H. Tagoshi, Phys. Rev. D **83**, 064003 (2011); **87**, 109901(E) (2013).
[106] S. Ossokine, T. Dietrich, E. Foley, R. Katebi, and G. Lovelace, Phys. Rev. D **98**, 104057 (2018).
[107] T. Chu, H. Fong, P. Kumar, H. P. Pfeiffer, M. Boyle, D. A. Hemberger, L. E. Kidder, M. A. Scheel, and B. Szilagyi, Classical Quantum Gravity **33**, 165001 (2016).
[108] Black Hole Perturbation Toolkit, https://bhptoolkit.org.